



Contents lists available at ScienceDirect



Applied Catalysis A: General

journal homepage: www.elsevier.com/locate/apcata

Steam reforming of ethanol for hydrogen production over MgO-supported Ni-based catalysts

Gleicielle T. Wurzler^{a,b}, Raimundo C. Rabelo-Neto^a, Lisiane V. Mattos^c, Marco A. Fraga^{a,b}, Fábio B. Noronha^{a,b,*}

^a National Institute of Technology, Catalysis Division, Av. Venezuela 82, Rio de Janeiro 20081-312, Brazil

^b Military Institute of Engineering, Chemical Engineering Department, Praça Gal. Tibúrcio 80, Rio de Janeiro 22290-270, Brazil

^c Fluminense Federal University, Chemical Engineering Department, Rua Passo da Pátria, 156, Niterói 24210-240, Brazil

ARTICLE INFO

Article history:

Received 13 July 2015

Received in revised form 5 November 2015

Accepted 11 November 2015

Available online xxx

Keywords:

Hydrogen production

Steam reforming of ethanol

Ni/MgO catalyst

Deactivation mechanism

ABSTRACT

This work studied the effect of preparation method of MgO on the performance of Ni/MgO catalysts for steam reforming of ethanol. Three different MgO were prepared by precipitation and aging, precipitation and decomposition of precursor salt. Depending on the synthesis conditions, the basicity and the type of Ni species significantly varied. TPD of adsorbed CO₂ showed that the MgO prepared by precipitation and aging possess the highest amount of basic sites. TPR and XANES revealed the presence of two different Ni species: NiO particles and Ni²⁺ inserted in the lattice of a NiO-MgO solid solution, which is hardly reducible. Ni supported on MgO obtained by precipitation and aging exhibited the highest reduction degree. The preparation method of MgO also affected the amount of carbon formed during SR of ethanol at 773 K under H₂O/ethanol molar ratio of 3.0. Increasing basicity decreased the amount of carbon deposits, which was attributed to the increase of carbon gasification rate.

© 2015 Elsevier B.V. All rights reserved.

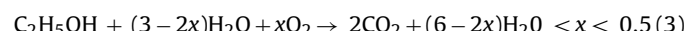
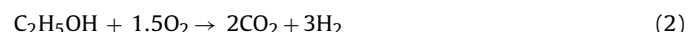
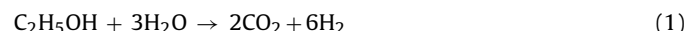
1. Introduction

Today, the majority of hydrogen is produced in refineries to upgrade crude oil (hydrocracking and hydrotreating process), in the petrochemical industry to synthesize different chemical compounds (such as ammonia and methanol), for oil and fat hydrogenation and, in metallurgical processes (as a reduction gas) [1]. However, the rising concern with the reduction of greenhouse gas emissions and atmospheric pollution increased the interest in using hydrogen as an energy carrier for power generation with fuel cells as well as for the conversion of biomass into liquid fuels.

Hydrogen can be electrochemically converted in PEM fuel cells to produce electricity for use in transportation applications and portable power devices and also for residential combined heat and power systems [2]. Hydrogen is also required in the hydrodeoxy-genation (HDO) process of bio-oil produced from the fast pyrolysis of biomass for gasoline and diesel production [3] as well as in HDO of fermentation products obtained in a sugarcane biorefinery for jet fuel and lubricants production [4].

Hydrogen can be produced through the steam reforming of biomass-derived liquids such as bioethanol, a water and ethanol mixture that may be obtained by biomass fermentation [5–8]. The steam reforming of ethanol is an attractive route to hydrogen production because: (i) it is a renewable and CO₂-neutral source that can readily be obtained from biomass fermentation; (ii) ethanol is significantly less toxic than methanol and gasoline; (iii) the infrastructure required for ethanol production and distribution is already established in countries like Brazil and USA since ethanol is currently distributed and blended with gasoline.

Different technologies may be applied to generate hydrogen from ethanol, including steam reforming (SR) (Eq. (1)), partial oxidation (POX) (Eq. (2)), and oxidative steam reforming (OSR) (Eq. (3)) [8]:



However, various reaction pathways may occur depending on the reaction conditions and the choice of the catalyst. Some of these reactions lead to the formation of coke and, consequently, induce catalyst deactivation.

The type of support directly influences the product distribution and catalyst stability during ethanol conversion reactions since it

* Corresponding author at: National Institute of Technology, Catalysis Division, Av. Venezuela 82, 20081-312 Rio de Janeiro, Brazil. Fax: +55 21 2123 1166.

E-mail address: fabio.bellot@int.gov.br (F.B. Noronha).

also exhibits activity for this reaction. Al_2O_3 is generally used as a support but its acid sites promote the dehydration of ethanol to ethylene, which is considered a precursor of coke [9]. MgO contains strong basic sites, which are proposed to be highly active for ethanol dehydrogenation to acetaldehyde that is considered the primary intermediate of SR of ethanol [9]. It is well known that basic metal oxides minimize carbon formation increasing adsorption of water and promoting the rate of carbon gasification reaction [10]. Therefore, there are many studies in the literature about the SR of ethanol over MgO supported catalysts [9,11–20]. However, carbon formation is still observed for SR of ethanol over Ni/MgO catalysts [11–15,18–20]. In fact, there is no work in the literature that studies the influence of the basic properties of magnesia on the rate of carbon formation during SR of ethanol. Then, the design of a catalyst resistant to carbon formation for SR of ethanol requires a better understanding of the effect of the surface basic properties of magnesia on catalyst deactivation. This can be done by tailoring the surface basic properties of magnesia and, consequently, the amount and strength of basic sites, by controlling the synthesis method. Menezes et al. [21] studied the effect of the preparation method on the surface basicity of MgO . Different MgO were synthesized by precipitation and hydrothermal treatments and decomposition of magnesium nitrate. The samples presented different basic site distributions, revealing the important role of the preparation conditions on tuning the surface basicity.

Therefore, the aim of this work is to study the effect of preparation method of MgO on the performance of Ni/MgO catalysts during ethanol conversion reactions. MgO was prepared by precipitation, precipitation with aging and decomposition of the precursor salt in order to vary the surface basicity. A correlation was established between the density of basic sites and the catalyst resistance to carbon deposition.

2. Experimental

2.1. Catalyst preparation

The MgOpa sample was prepared by precipitation followed by aging. $\text{Mg}(\text{NO}_3)_2 \cdot 6\text{H}_2\text{O}$ and NaOH solutions were slowly added to a Na_2CO_3 solution under vigorous stirring. The precipitate formed was aged at pH 10 for 12 h. The gel was centrifuged and extensively washed with distilled water until constant pH. Then, it was dried at 373 K for 12 h and calcined at a heating rate of 5 K/min up to 773 K for 5 h.

Another sample (MgOp) was also synthesized by precipitation from the same $\text{Mg}(\text{NO}_3)_2 \cdot 6\text{H}_2\text{O}$ and Na_2CO_3 precursors. In this case, an aqueous solution of $\text{Mg}(\text{NO}_3)_2 \cdot 6\text{H}_2\text{O}$ was quickly added to a container with the base solution. The magnesium hydroxide precipitate was formed instantly. It was then filtered, washed with distilled water until no pH change could be detected, and then calcined at 773 K for 5 h (5 K/min).

A third sample (MgOd) was obtained by thermal decomposition of $\text{Mg}(\text{NO}_3)_2$ in a muffle at 773 K for 5 h.

The catalysts were prepared by incipient wetness impregnation of the supports with an aqueous solution of $\text{Ni}(\text{NO}_3)_2 \cdot 6\text{H}_2\text{O}$ (Sigma-Aldrich) to obtain 5 wt% Ni. The samples were dried at 373 K and calcined under air (50 mL/min) at 673 K for 3 h. Three catalysts were obtained: Ni/MgOpa, Ni/MgOp, Ni/MgOd.

2.2. Catalyst characterization

2.2.1. X-ray fluorescence spectrometry (XRF)

The chemical composition of each sample was determined on Wavelength Dispersive X-Ray Fluorescence Spectrometer (WD-XRF) S8 Tiger, Bruker with a rhodium tube operated at 4 kW. The

analyses were performed with the samples (300 mg) in powder form using a semi-quantitative method (QUANT-EXPRES/Bruker).

2.2.2. X-ray diffraction (XRD)

The X-ray powder diffraction pattern of the calcined samples were obtained with $\text{Cu K}\alpha = 1,5406^\circ$ using a RIGAKU diffractometer. Data were collected over the 2θ range of 30° – 130° using a scan rate of $0.02^\circ/\text{step}$ and a scan time of 1 s/step. The lattice parameters of MgO and NiO were calculated from the (200) reflections (Eq. (4)). The composition of the $\text{NiO}-\text{MgO}$ solid solution was calculated from Vegard's rule (Eq. (5)) [22]. The Scherrer equation was used to estimate the crystallite mean diameter of MgO and metallic Ni particles (Eq. (6)).

$$a = \frac{\sqrt{h^2 + k^2 + l^2} \times \lambda}{2 \sin \theta} \quad (4)$$

$$a_{\text{Ni}_x\text{Mg}_{1-x}\text{O}} = x \times a_{\text{NiO}} + (1 - x) \times a_{\text{MgO}} \quad (5)$$

$$d = \frac{k \times \lambda}{\beta \times \cos \theta} \quad (6)$$

where a is the lattice parameter; h , k and l are the Miller indices; λ is the wave length; θ is the diffraction angle; x is the composition of the $\text{NiO}-\text{MgO}$ solid solution; d is the crystallite size; k is a constant (0.9); and β is the width at half-maximum intensity of the diffraction line.

In situ XRD was carried out at the XPD-10B beamline of the Brazilian Synchrotron Light Laboratory (LNLS). The samples were placed in a furnace installed into a Huber goniometer operating in Bragg-Brentano geometry ($\theta - 2\theta$). The XRD patterns were obtained by a Mythen-1 K detector (Dectris) located 1 m from the furnace, in a 2θ interval from 23° to 56° , using a wavelength of 1.55002 Å. The measurements were made while the sample underwent the following conditions: (i) Reduction under a 5% H_2/He mixture from 298 to 1023 K at a heating of 10 K/min, remaining at this temperature for 1 h. After reduction the sample was purged with helium at the same temperature for 30 min (ii) SR of ethanol—reaction mixture containing 98% He, 1.5% H_2O , 0.5% ethanol for at 773 K for 1 h. The average crystallite size of metallic Ni for the reduced catalyst and for the used catalyst after SR of ethanol reaction was calculated using the Scherrer equation (Eq. (6)). An Omnistar/Pfeiffer Vacuum mass spectrometer (MS) was used for on-line monitoring of effluent gas composition.

2.2.3. Temperature-programmed desorption of CO_2 (TPD- CO_2)

The basic surface sites were probed by temperature programmed desorption of adsorbed CO_2 . TPD- CO_2 was carried out in a fixed-bed reactor coupled to a quadrupole mass spectrometer (Balzers). Prior to TPD analyses, the samples were treated under flowing H_2 (30 mL/min) up to 1023 K (10 K/min), remaining at that temperature for 1 h. The system was then purged with flowing He at the treatment temperature for 30 min and cooled to room temperature. The adsorption of CO_2 was performed at room temperature by flowing CO_2 through the sample. Then, the sample was purged under He for 30 min. After adsorption, the catalyst was heated at a heating rate of 20 K/min up to 773 K in flowing He (50 mL/min).

2.2.4. Temperature programmed reduction (TPR)

TPR experiments were performed in a TPR/TPD 2900 Micromeritics system equipped with a thermal conductivity detector (TCD). The catalyst was pretreated at 473 K for 1 h under a flow of air prior to the TPR experiment in order to remove adsorbed species from the catalyst surface. The reducing mixture (10% H_2/N_2) was passed through the sample (100 mg) at a flow rate of 30 mL/min and the temperature was increased to 1273 K at a heating rate of 10 K/min.

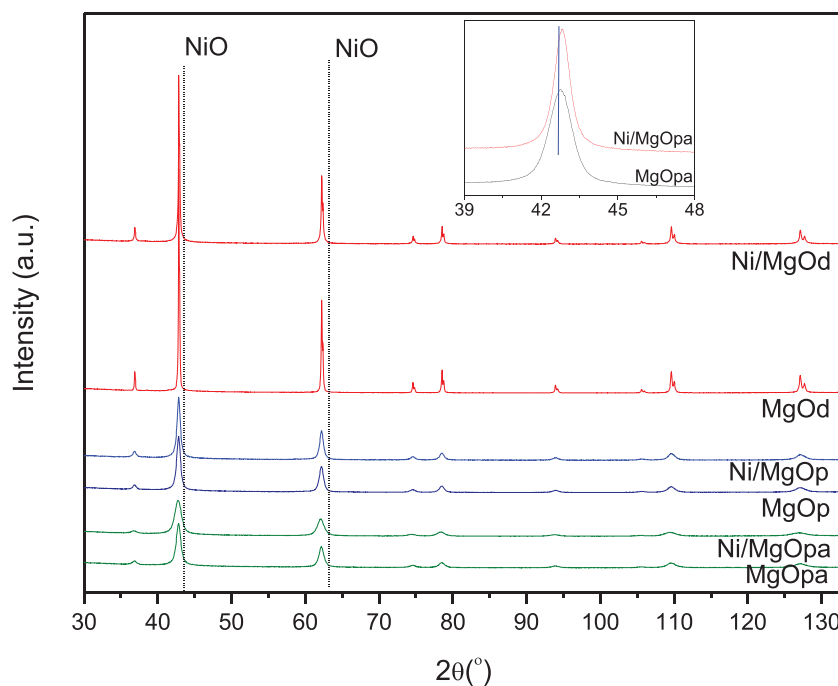


Fig. 1. XRD patterns of calcined MgO and Ni/MgO samples.

2.2.5. In-situ XAFS

In-situ XAS experiments were performed at the D08B-XAFS-2 beamline of the Brazilian Synchrotron Light Source (LNLS, Campinas). The samples were previously reduced under pure H₂ at 1023 K for 1 h and then passivated with a 5% O₂/He mixture for 1 h at 209 K as previously described for XRD experiments. Then, the samples were packed into a 1.0 (I.D.) x 1.2 (O.D.) mm capillary reactor, placed inside a furnace, whose temperature was controlled *via* a thermocouple placed inside the reactor right close to the catalyst bed. Ni K-edge spectra were recorded in the transmission mode, while the sample underwent the following treatment: (i) heating ramp under a 5% H₂/He mixture at 10 K min⁻¹ up to 1023 K, (ii) temperature hold for 30 min at 1023 K, (iii) sample cooling down to room temperature, under a 5% H₂/He mixture flow. Data reducing was made using the ATHENA software package [23]. The background subtracted, normalized XANES spectra were then trimmed at a suitable energy range (c.a.100 eV above the absorption edge). The composition of metallic Ni phase during sample activation (reduction under H₂/He flow) was monitored by linear combination of normalized Ni K-edge XANES spectra (LC-XANES) within the 8.3–8.43 keV energy range, using Ni foil, NiO and a solid solution NiMgO as references for Ni⁰ and Ni²⁺, respectively.

2.2.6. Thermogravimetric analysis (TG)

Thermogravimetric analysis of the used catalysts was carried out in a TA Instruments equipment (SDT Q600) in order to determine the amount of carbon formed over the catalyst. Approximately 10 mg of spent catalyst was heated under air flow from room temperature to 1273 K at a heating rate of 20 K/min and the weight change was measured.

2.2.7. Scanning electron microscopy (SEM)

SEM analyses of the spent catalysts were carried out using a field emission scanning electron microscope (FE-SEM) Quanta FEG 450 FEI operating with an accelerating voltage of 20 kV. The microscope was also equipped with an EDAX analytic system energy dispersive spectrometer (Oxford Instruments—model X-MAX).

2.3. SR and OSR of ethanol

SR and OSR of ethanol reactions were performed in a quartz tube reactor at 773 K and atmospheric pressure. Prior to reaction, samples were reduced under pure hydrogen (30 mL/min) at 1023 K for 1 h and then purged with N₂ at the same temperature for 30 min. For SR, H₂O/ethanol molar ratio of 3.0 and 10.0 were used. The reactant mixture was obtained by flowing two N₂ streams (30 mL/min) through each saturator containing ethanol and water separately. OSR was performed employing a H₂O/ethanol molar ratio of 3.0 and an O₂/ethanol molar ratio of 0.5. A flow of 5.6% O₂/N₂ (30 mL/min) and a flow of N₂ (30 mL/min) were passed through the saturators containing ethanol and water, respectively. The partial pressure of ethanol was maintained constant for all experiments. In order to observe the deactivation of the catalyst within a short timeframe, a small amount of catalyst was used (20 mg). The samples were diluted with inert SiC (SiC mass/catalyst mass = 3.0). The reaction products were analyzed by gas chromatography (Micro GC Agilent 3000 A) containing three channels for three thermal conductivity detectors (TCD) and three columns: a molecular sieve, a Poraplot Q and OV-1 column. The ethanol conversion and products distribution were determined as follows:

$$X_{\text{ethanol}} = \frac{(n_{\text{ethanol}})_{\text{fed}} - (n_{\text{ethanol}})_{\text{exit}}}{(n_{\text{ethanol}})_{\text{fed}}} \times 100 \quad (7)$$

$$S_x = \frac{(n_x)_{\text{produced}}}{(n_{\text{total}})_{\text{produced}}} \times 100 \quad (8)$$

where (n_x)_{produced} = moles of x produced (x = hydrogen, CO, CO₂, methane, acetaldehyde or ethene) and (n_{total})_{produced} = moles of H₂ + moles of CO + moles of CO₂ + moles of methane + moles of acetaldehyde + moles of ethene (the moles of water produced are not included).

Table 1

Chemical composition of Ni/MgO catalysts and BET surface area of the supports.

Catalyst	Chemical composition (%)		Support surface area (m ² /g)
	NiO (Ni ⁰)	MgO	
Ni/MgOpa	6.75 (5.30)	93.25	149
Ni/MgOp	6.58 (5.17)	93.42	71
Ni/MgOd	7.18 (5.64)	92.82	3

Composition of metallic Ni in parentheses.

3. Results and discussion

3.1. Catalyst characterization

Table 1 presents the NiO (Ni⁰ in parentheses) and MgO content of all samples. The Ni loading obtained by XRF analysis was close to the nominal value for all samples studied (5.0 wt.% Ni). Furthermore, traces of sodium were not detected.

Fig. 1 shows the XRD patterns of the supports prepared by different methods. The diffractograms of all samples exhibited the diffraction lines characteristic of the periclase MgO phase with cubic structure (PDF#45-0946). However, sharper lines were registered for MgOd, indicating that this sample presented the highest crystallinity.

The XRD patterns of the Ni/MgO obtained after calcination (**Fig. 1**) were quite similar to those of the parent supports, showing the lines corresponding to the periclase MgO phase with cubic structure as well. It was not possible to distinguish the NiO phase (PDF#47-1049). Nevertheless, when the diffractograms of Ni/MgO were compared to the diffractograms of the respective supports, it was observed that the lines of MgO phase were shifted to higher 2θ positions. The lattice constant *a* of MgO and Ni/MgO was calculated from the (200) reflections and listed in **Table 2**. The results obtained were in agreement with data reported in the literature [24–26]. Regardless the MgO preparation method, the addition of Ni decreased the lattice constant. Accordingly, [24–30], the shift of the MgO peak position towards higher 2θ positions and the decrease in the MgO lattice constant suggests the formation of a NiO–MgO solid solution during calcinations for all samples. The composition of the Ni_xMg_{1-x}O solid solution formed was estimated based on Vegard's rule [22] and the results were reported in **Table 2**. For Ni/MgOp and Ni/MgOd, these values were close to the theoretical one (*x* = 0.035), whereas it was higher for Ni/MgOpa. This result was also obtained by Arena et al. [26] and it was attributed to a gradient of Ni²⁺ across the MgO particle. The crystallite size of MgO was calculated using the line corresponding to (200) reflection and the results obtained are listed in **Table 2**. MgOpa exhibited the smallest MgO crystallite size (8.4 nm), whereas the largest value was found for MgOd (46.5 nm). In the case of Ni/MgO samples prepared by hydrothermal and precipitation methods, the addition of Ni slightly increased the MgO crystallite size. For the sample synthesized by decomposition, the MgO crystallite size slightly decreased.

Table 2Diffraction angle, lattice parameter, composition of the Ni_xMg_{1-x}O solid solution and crystallites size of MgO obtained for all calcined samples.

Samples	Difraction angle 2θ (°)	<i>a</i> ^a (Å)	Solid ^b solution composition	<i>d</i> ^c (nm)
MgOpa	42.779	4.2263	–	8.4
MgOp	42.827	4.2218	–	16.3
MgOd	42.846	4.2200	–	46.5
Ni/MgOpa	42.812	4.2229	Ni _{0.066} Mg _{0.934} O	13.0
Ni/MgOp	42.844	4.2202	Ni _{0.038} Mg _{0.962} O	19.2
Ni/MgOd	42.860	4.2187	Ni _{0.032} Mg _{0.968} O	44.3

^a Lattice constant.^b Solid solution composition calculated from Vegard's rule: $a_{Ni_xMg_{1-x}O} = x \cdot a_{NiO} + (1-x) \cdot a_{MgO}$.^c Crystallite size of MgO calculated using the (200) plane.

The TPR profile of MgO supported catalysts and NiO reference were shown in **Fig. 2**. Ni/MgOpa catalyst exhibited three peaks at 555, 725 and 956 K. The reduction profiles of Ni/MgOd and Ni/MgOp exhibited peaks at 565 and 587 K, respectively, and at 943 and 1055 K, respectively, and a shoulder at around 710 K. The assignment of reduction peaks of Ni-based catalysts remains controversial in the literature and this is likely due to the differences in the experimental conditions applied for the analysis and in the synthesis method used to obtain the samples. For example, the TPR profile of bulk NiO exhibit peaks at 589 K [31], 593 K [32], 600 K [33], 693 K [34], or a peak and a shoulder at 662/723 K [35] or at 715/770 K [36]. In the present work, the TPR profile of NiO showed a peak at 718 K and a shoulder at around 748 K (**Fig. 2**).

There are some studies in the literature that report the TPR profile of Ni/MgO catalyst [37,38]. The reduction profile of 21% Ni/MgO showed two peaks at 553 and 973 K that were attributed to the reduction of NiO particles and Ni²⁺ ions located in the MgO lattice, revealing the presence of a NiO–MgO solid solution [37]. Parmaliana et al. [38] carried out a systematic study about the effect of the calcination temperature (673–1273 K) and nickel loading (2.8, 10.8 and 18.0 wt.% Ni) on the reduction of Ni/MgO catalysts using TPR. The reduction profile of Ni/MgO calcined at 673 K exhibited 3 peaks and a shoulder. The small peak at 533 K was attributed to the presence of Ni³⁺ species. The peak at 613 K was associated with bulk NiO on the surface of MgO. The peak at 863 K and the shoulder at 1011 K were assigned to Ni²⁺ located in the outermost and inner layers of the MgO lattice. When the calcination temperature was increased, the low temperature peak disappeared. In addition, the peak corresponding to bulk NiO was shifted to higher temperatures, indicating that the interaction of NiO with MgO increased, probably forming a NiO–MgO solid solution. This peak was no longer detected after calcination at 1073 K. The peak at high temperature increased and it was shifted to higher temperature. This result reveals that the increase of calcination temperature favors the diffusion of NiO into MgO lattice, promoting the formation of a NiO–MgO solid solution and, consequently, the reduction of Ni²⁺ becomes more difficult. The reducibility of Ni/MgO catalysts decreases when the metal loading decreases. For the sample containing 2.8% Ni, only a broad peak at high temperature is observed in the TPR profile.

Taking into account the peak assignments of TPR profiles of Ni catalysts from the literature, the types of Ni species on Ni/MgO catalysts of our study were identified. Therefore, the peak at 725 K in the TPR profile of Ni/MgOpa could be attributed to the reduction of bulk NiO particles (**Fig. 2**). In our work, the diffractograms did not detect the presence of NiO phase. However, further evidence for the formation of NiO particles was provided by linear combination of normalized Ni K-edge XANES spectra that will be presented in the next session. The broad consumption of hydrogen at 956 K might be assigned to the reduction of Ni²⁺ cations inserted into the lattice of MgO due to the formation of a solid solution during calcination, as it was demonstrated by XRD data. The low reduction peak deserves additional comments. Ewbank et al. [39] performed a comprehen-

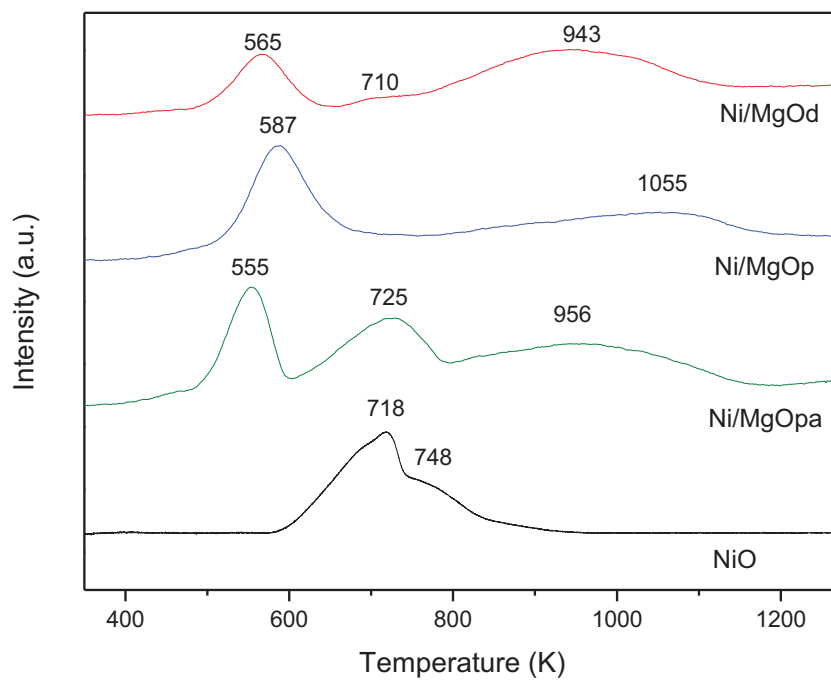


Fig. 2. TPR profiles of Ni/MgO catalysts.

Table 3
Hydrogen consumption from TPR profiles.

Sample	H ₂ consumption(area%)		Total H ₂ uptake (μmol/g)	Degree of reduction (%)
	600–800 K	>800 K		
Ni/MgOpa	47	53	87	74
Ni/MgOp	11	89	55	31
Ni/MgOd	5	95	40	42

sive study about the nature of the Ni species in Ni/Al₂O₃ catalysts prepared by controlled adsorption and dry impregnation. TPR profile exhibited several peaks depending on the catalyst preparation method. The first peak appeared at 523 and 613 K for the samples prepared by dry impregnation and controlled adsorption, respectively. This peak was attributed to the decomposition of residual nitrate. This low temperature peak at 490 K in the TPR profile of 10% Ni/CeO₂ was also assigned to the decomposition of residual nitrates [40]. Sheffer et al. [33] also reported the presence of a peak at 570 K in the reduction profile of Ni/Al₂O₃ catalysts that was attributed to the decomposition and reduction of nitrates.

In order to shed more light on the reduction peak at low temperature, the reduction treatment was followed by mass spectrometry coupled to the same set up used to perform the *in situ* XRD experiments that will be described next.

Signals corresponding to NO₂, NO or NH₃ were not detect during treatment under H₂/He mixture. However, an intense signal due to CO₂ was clearly observed at the same temperature of the first peak in the TPR profile. This results suggests that residual carbonates decompose in this temperature range and could be responsible for the peaks observed in the temperature range of 555–587 K for Ni/MgO catalysts. In fact, the CO₂-TPD experiments revealed the desorption of carbonate species above 673 K and thus, they could remain adsorbed on the support even after the pretreatment carried out before the TPR experiment.

The H₂ consumption of TPR profiles are listed in Table 3. Since the first peak corresponds to the decomposition of residual carbonates species, not only might the evolution of hydrogen occur but also CO₂ [39]. This compound could contribute to the TCD signal

as well and then, the H₂ consumption in this temperature region was not taken into account in the total hydrogen uptake values reported in Table 3. Comparing the catalysts prepared from MgO obtained by different methods, it is observed that the fraction of hydrogen uptake at high temperature is higher on Ni/MgOp and Ni/MgOd catalysts, indicating a higher formation of solid solution. Ni/MgOpa catalyst revealed a higher fraction of bulk NiO particles. This might explain the higher reduction degree observed for this sample.

In order to confirm the peak assignments of TPR profiles of our Ni/MgO catalysts, *in situ* H₂-TPR XAFS studies were performed at Ni K-edge.

3.2. In situ characterization

Fig. 3a shows the TPR-XANES spectra near the Ni K-edge for Ni/MgOpa catalyst. Increasing the temperature under H₂ flow up to 573 K did not change the spectra. This result is in agreement with TPR profile that showed only the decomposition of carbonates in this temperature range. Further increase in the temperature caused the decrease in the intensity of the white line in XANES spectra, indicating the progressive reduction of Ni²⁺ species.

Fig. 3b displays the evolution of the Ni species during reduction determined by the linear combination of normalized Ni K-edge XANES spectra, using Ni foil, NiO and a solid solution NiMgO as references. Initially, nickel is mainly in the Ni²⁺ oxidation state in the structure of the solid solution. Only a small fraction is present as NiO phase, which agrees well with the TPR results (Table 3). The reduction of NiO to metallic Ni started at around 573 K, whereas the Ni²⁺ in the solid solution is reduced at higher temperatures (above 773 K), in agreement with TPR experiments. The fraction of metallic Ni steadily increased up to the final reduction temperature (1023 K), and continuously increased during 1 h at 1023 K (Fig. 3b).

The XANES spectra of Ni-K-edge after reduction at 1023 K for 1 h of all Ni/MgO catalysts and references are shown in Fig. 4. The presence of an intense white line for all catalysts is quite clear, indicating that the reduction of all samples was not com-

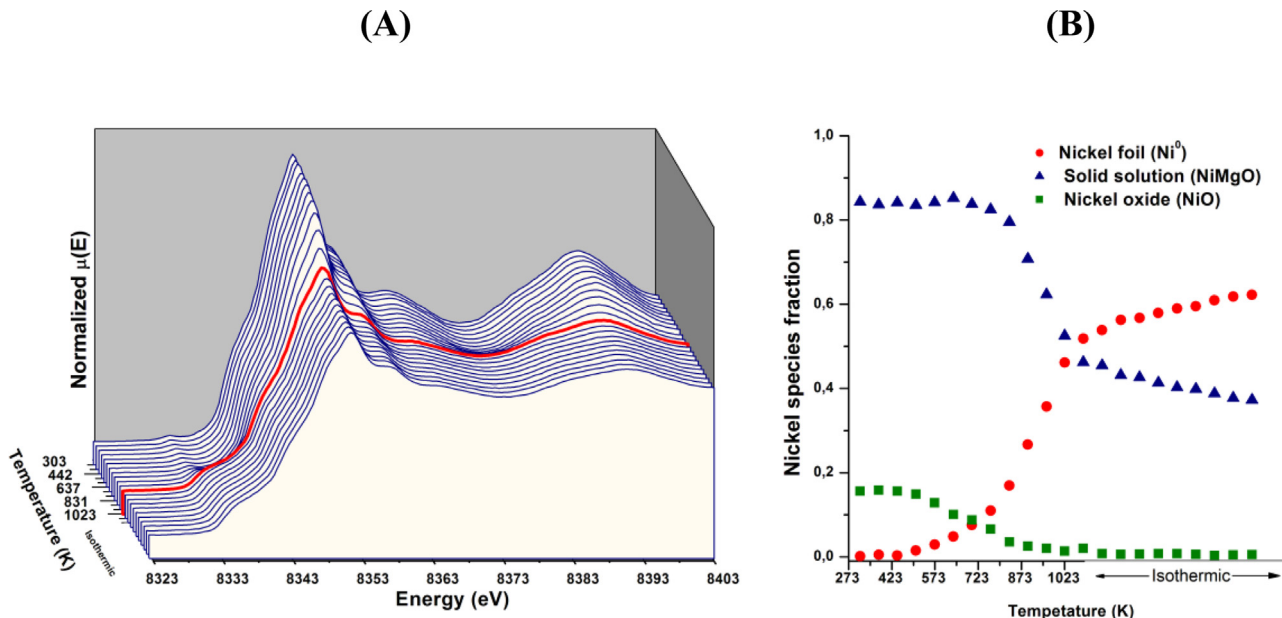


Fig. 3. (A) *In situ* XANES spectra and (B) LC-XANES of Ni/MgOpa catalyst during reduction under 5% H₂/He flow.

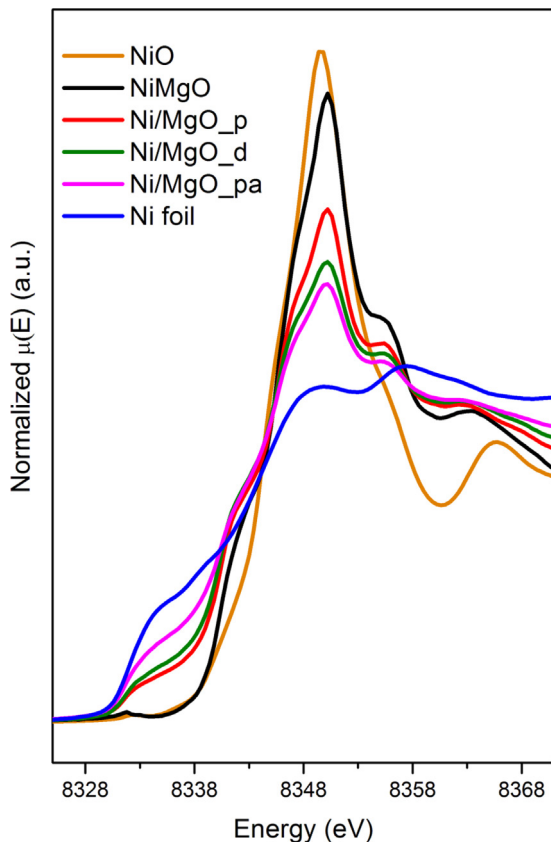


Fig. 4. *In situ* XANES spectra of MgO supported Ni after reduction at 1023 K and Ni⁰ and NiMgO references.

plete. The distribution of Ni species after reduction of all samples at 1023 K was determined by linear combination of normalized Ni K-edge XANES spectra (LC-XANES) using Ni foil, NiO and a solid solution NiMgO as references for Ni⁰ and Ni²⁺, respectively (Table 4). These result showed the presence of metallic Ni and Ni²⁺ in the solid solution on the reduced samples. Considering that the TPR experiments revealed the existence of NiO and NiMgO

Table 4

Fraction of metallic Ni and Ni in the solid solution after reduction at 1023 K calculated by the linear combination of Ni K-edge XANES spectra of references.

Sample	% Ni ⁰	% Solid solution
Ni/MgOpa	61	39
Ni/MgOp	37	63
Ni/MgOd	50	50

solid solution for all calcined samples, LC-XANES indicate that NiO was completely reduced to metallic Ni whereas only partial reduction of the NiMgO solid solution took place. In addition, Ni/MgOpa catalyst exhibited the highest percentage of metallic Ni, which agrees very well with the TPR discussion presented hereinbefore.

The diffractograms obtained during the reduction of Ni/MgOpa sample under the 5% H₂/He mixture are shown in Fig. 5A. The diffractogram of the calcined sample exhibited lines located at $2\theta = 37.2$ and 43.1° suggesting the formation of a NiO–MgO solid solution. There are also lines at $2\theta = 38.3$ and 51.1° corresponding to Mg(OH)₂ phase, which disappeared when the temperature was increased. By raising the temperature, typical lines corresponding to MgO were shifted to lower 2θ positions. For example, the line positioned at $2\theta = 43.1^\circ$ at 298 K moved to 42.8° after reduction at 1023 K. This result indicates that Ni was removed from the solid solution, generating metallic Ni particles, which were initially observed at around 873 K. It is noticed the presence of a shoulder at $2\theta = 44.1^\circ$ and a small peak at $2\theta = 51.4^\circ$ that corresponds to the diffraction lines characteristic of metallic Ni (1 1 1) and (2 0 0) planes (Fig. 5B, curve a). The diffractogram obtained after 1 h under SR of ethanol reaction remained unchanged (Fig. 5B, curve b).

For Ni/MgOp (Fig. 6) and Ni/MgOd (Fig. 7) samples, the diffractograms obtained were quite similar to that one of Ni/MgOpa (Fig. 5). The lines corresponding to MgO were also shifted to lower 2θ positions during the reduction, which suggested that the solid solution was partially destroyed. The lines characteristic of metallic Ni appeared at 1023 K (Ni/MgOp) and 973 K (Ni/MgOd). These temperatures are higher than that observed for Ni/MgOp, which agrees very well with the lower reduction degree of these samples as calculated by TPR (Table 3).

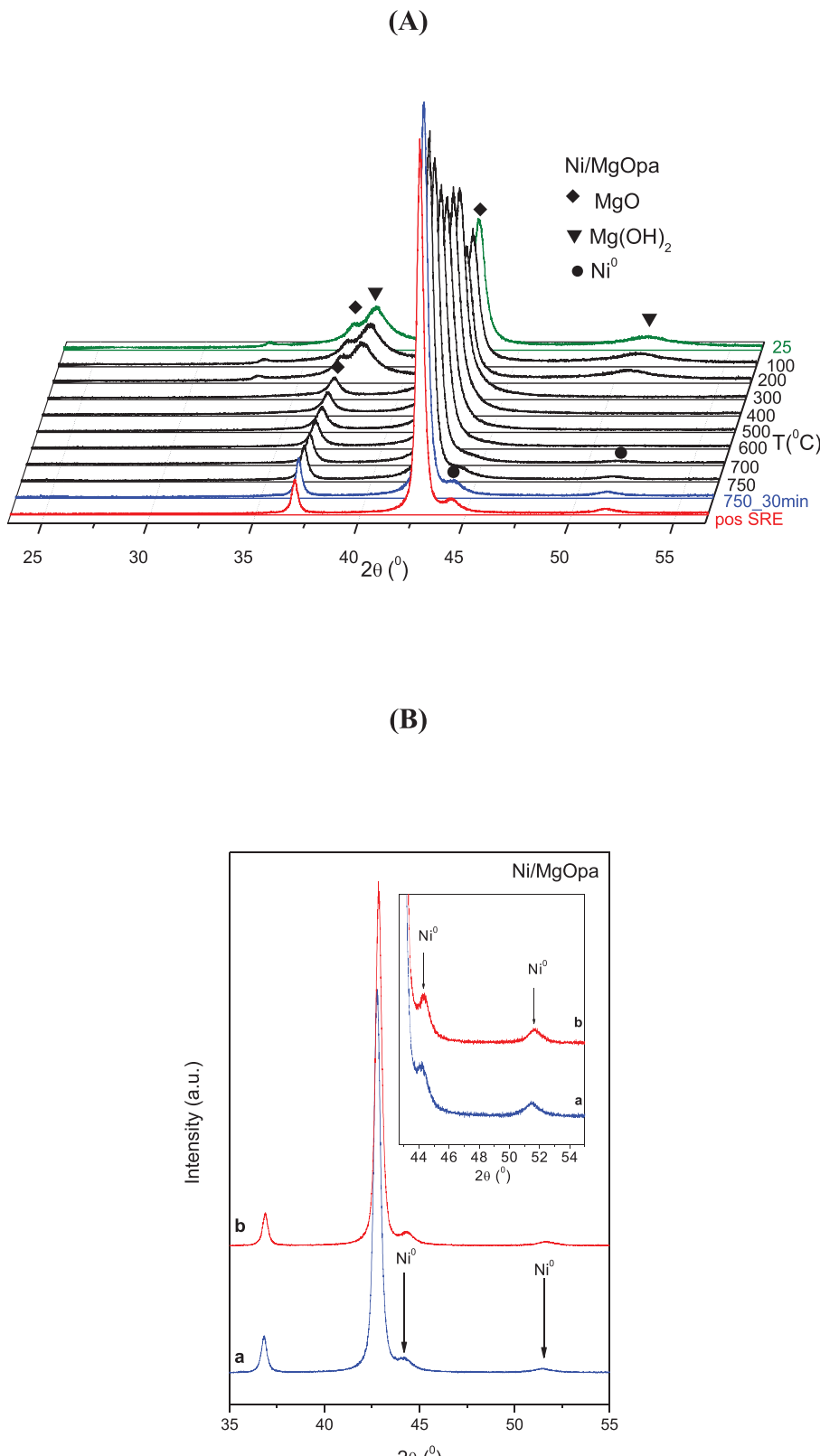


Fig. 5. (A) Diffractograms of Ni/MgOpa obtained during reduction at different temperatures; (B) XRD diffraction patterns of (a) reduced sample; (b) after SR of ethanol reaction at 773 K.

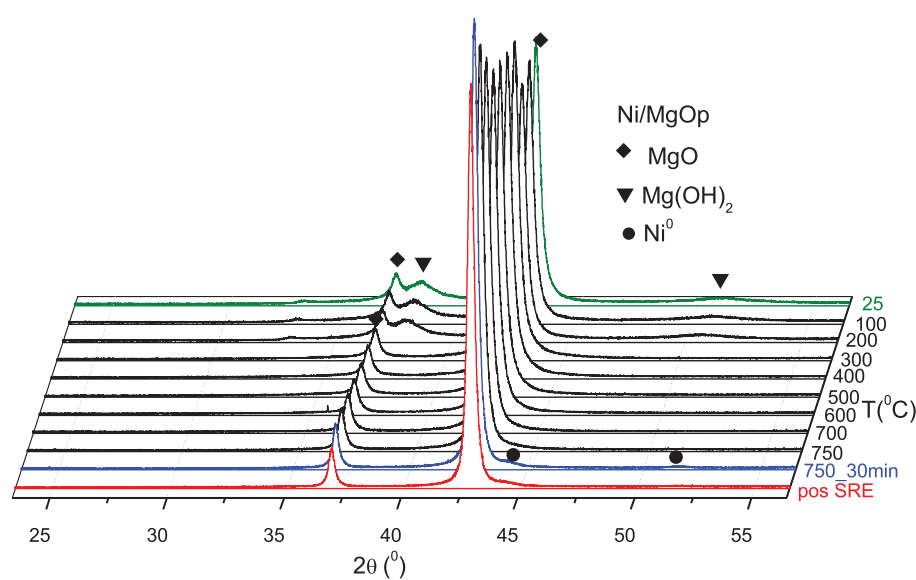
3.3. Characterization of surface basic sites

A qualitative analysis of the distribution of basic sites (*i.e.*, strength and population) can be obtained by TPD of adsorbed CO_2 (Fig. 8). All samples presented a rather complex profile with more

or less resolved multiple peaks between 300 and 800 K, suggesting a wide distribution of basic sites.

The desorption profile of CO_2 have been related to the distribution of basic sites, including both density and strength [41–43]. Cosimo et al. [42] associated the different species of adsorbed CO_2

(A)



(B)

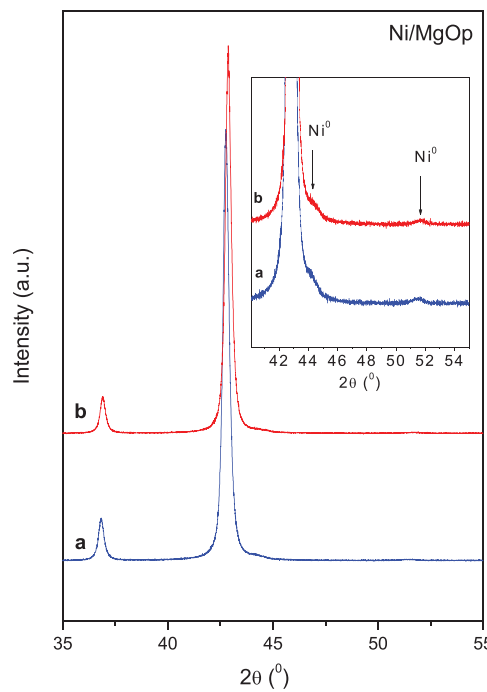
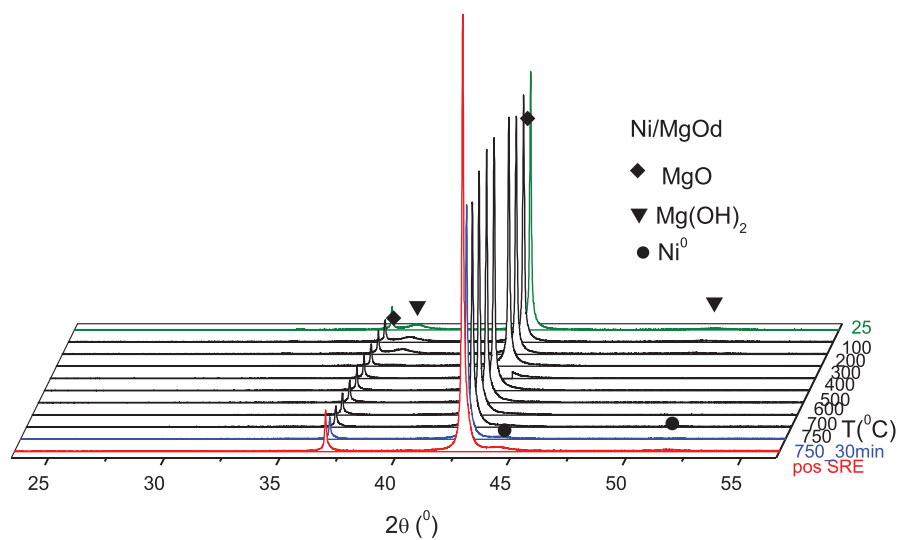


Fig. 6. (A) Diffractograms of Ni/MgOp obtained during reduction at different temperatures; (B) XRD diffraction patterns of (a) reduced sample; (b) after SR of ethanol reaction at 773 K.

on MgO, Al₂O₃ and Mg-Al mixed oxides to different types of surface basic sites. The low temperature desorption peak was correlated with hydrogen carbonate species adsorbed on weakly basic OH groups (low basic strength site), while bidentate carbonates were

suggested to be adsorbed on Mg-O site pairs of moderate basic strength, and finally monodentate carbonate was assigned to isolated O₂⁻ anions of high basic strength site, remaining adsorbed even at high temperature.

(A)



(B)

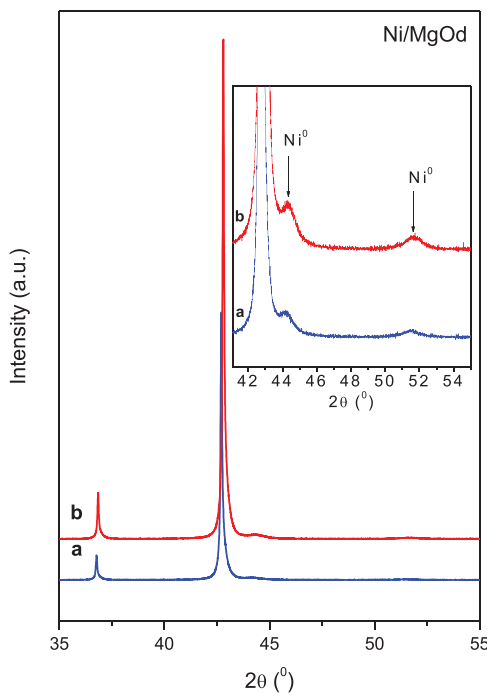


Fig. 7. (A) Diffractograms of Ni/MgOd obtained during reduction at different temperatures; (B) XRD diffraction patterns of (a) reduced sample; (b) after SR of ethanol reaction at 773 K.

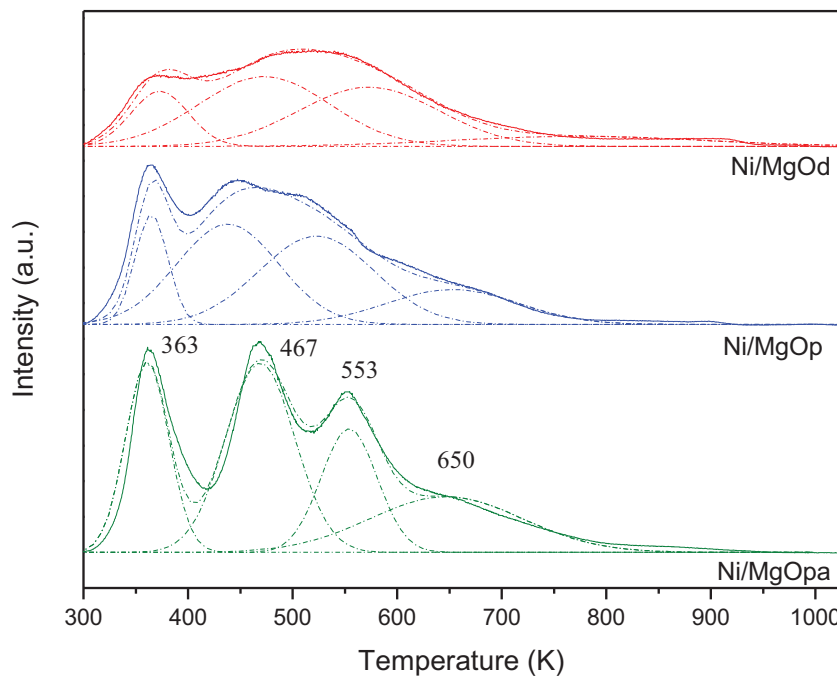


Fig. 8. TPD of CO_2 profiles of Ni/MgO catalysts.

Table 5

Distribution of weak, medium and strong surface basic sites and total amount of CO_2 desorbed.

Sample	Basic sites distribution (area%)			Total evolved CO_2 ($\mu\text{mol g}^{-1}$)
	Weak	Medium	Strong	
Ni/MgOpa	22	31	47	19966
Ni/MgOp	11	39	50	14801
Ni/MgOd	15	40	45	4575

Therefore, in this work, the peaks corresponding to the evolution of CO_2 during the TPD experiment can be related to the different carbonate species observed. The peaks at low temperature region (300 and 500 K) are assigned to decomposition of hydrogen carbonate and bidentate carbonate species, respectively, while the CO_2 released above 500 K is ascribed to the decomposition of monodentate and polydentate carbonate species. The relative contribution of each individual desorption peak was obtained by decomposition of the desorption curves, considering the adsorption of four different carbonate species. A multiple-Gaussian function was selected for fitting the experimental data. The experimental curve was fitted quite well as it was shown in Fig. 8. The quantitative data obtained by integrating the decomposed peaks are reported in Table 5. Regardless the MgO preparation method, all samples exhibited a higher fraction of high basic strength sites (monodentate and polydentate carbonate species). There is only a slight difference between the distribution of weak and medium basic strength sites. This result did not agree with the work of Menezes et al. [21], who reported significant differences in basic site distribution as a function of the MgO preparation method. The apparent contradictory results could be attributed to the pretreatment conditions. In the present work, the samples were previously reduced before the adsorption of CO_2 , which could expose or create coordinatively unsaturated sites that are responsible for the basicity of surface oxides. Ni could also promote the reduction of the support by hydrogen spill over from the metallic particle to the support. The total amount of basic sites were also calculated and listed in Table 6. The results showed that the preparation method of MgO

Table 6

Amount of carbon deposited on Ni/MgOpa, Ni/MgOp and Ni/MgOd catalysts after SR and OSR of ethanol at 773 K.

Sample	Reaction condition	$\text{mg C gcat}^{-1} \text{h}^{-1}$	$\text{mg C gcat}^{-1} \text{h}^{-1} \text{mole reacted ethanol}^{-1}$
Ni/MgOpa	SR 3:1	6.2	0.103
	SR 10:1	4.5	0.063
	OSR	0.3	0.003
Ni/MgOp	SR 3:1	6.2	0.163
Ni/MgOd	SR 3:1	6.9	0.230

significantly affected the amount of basic sites, following the order: Ni/MgOpa > Ni/MgOp > Ni/MgOd.

3.4. SR of ethanol over Ni/MgO catalysts

Ethanol conversion and product distributions as a function of time on stream (TOS) for SR of ethanol at 773 K over Ni/MgO catalysts are shown in Fig. 9. Ni/MgOpa exhibited the highest initial ethanol conversion, which is likely due to the higher reduction degree as revealed by TPR and XANES experiments. The main products formed were H_2 , CO_2 , CO, and CH_4 , indicating that SR of ethanol and ethanol decomposition are the main reactions taking place. Small amounts of acetaldehyde were also observed for Ni/MgOp (3%) and Ni/MgOd (5%) catalysts. The activity of the MgO supports for the SR of ethanol is low. In addition, H_2 , acetaldehyde and ethylene were the main products formed, suggesting that ethanol dehydrogenation and ethanol dehydration reactions are favored on the supports. Frusteri et al. [11] studied the performance of 3 wt% Rh/MgO, 3 wt% Pd/MgO, 21 wt% Ni/MgO, and 21 wt% Co/MgO catalysts for the SR of ethanol. These catalysts exhibited similar product distributions characterized mainly by H_2 , CO_2 , and CO. CH_4 and acetaldehyde were also observed. All catalysts deactivated whereas the supports remained quite stable during reaction. These results suggest that catalyst deactivation occurs on the surface of metallic particle or on the metal-support interface.

Catalyst deactivation during SR of ethanol is generally attributed to the deposition of carbonaceous species as well as either the sintering or oxidation of metallic particles [8]. Carbon formation

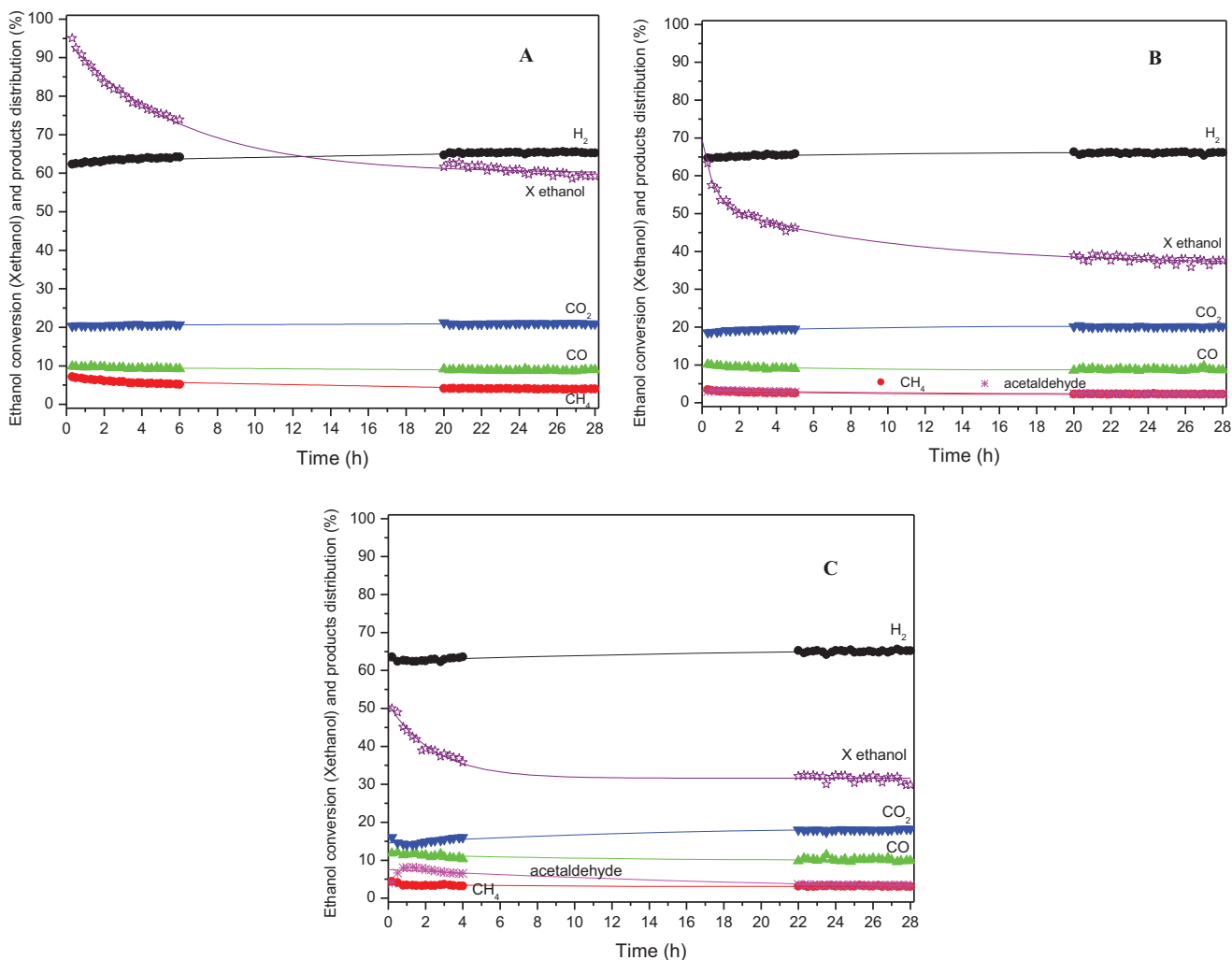


Fig. 9. Ethanol conversion and product distribution as a function of TOS for SR of ethanol at 773 K over Ni/MgO catalysts, using H₂O/ethanol molar ratio of 3.0. (A) Ni/MgOpa; (B) Ni/MgOp; (C) Ni/MgOd.

has been reported over Ni/MgO catalyst during SR of ethanol [11–15,18–20]. In order to investigate the main causes of Ni/MgO catalysts deactivation during SR of ethanol, SEM and TG of used catalysts and *in situ* XRD were carried out and the results obtained are discussed in the following section.

3.5. Characterization of post-reaction Ni supported catalysts

The SEM images of post-reaction catalysts showed the presence of carbon filaments for all Ni/MgO catalysts (Fig. 10). However, the extent of the formation of carbon filaments was very limited on Ni/MgOpa. From TG analysis, the amount of carbon deposited on Ni/MgO catalysts prepared by different methods was calculated and the results are listed in Table 6.

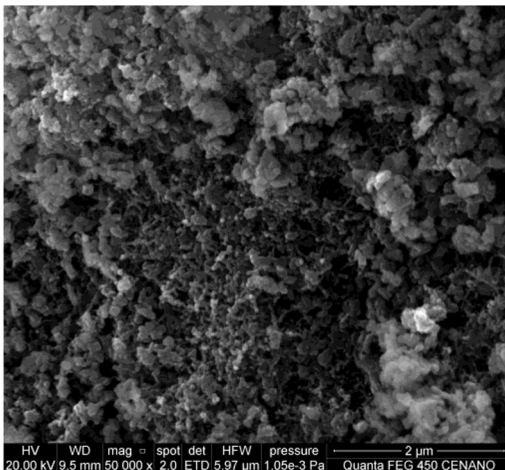
After SR of ethanol at 773 K, the amount of carbon formed was approximately the same for all catalysts (6.2–6.9 mgC/gcat/h). However, any comparison concerning the amount of carbon formed between all samples is somewhat hampered by the fact that the samples present rather different deactivation behavior. Then, the amount of carbon deposited was calculated in mgC/gcat/h/mol of converted ethanol and the results are listed in Table 6. The amount of carbon deposited was significantly affected by the preparation method of MgO. The lowest carbon deposition was observed on Ni/MgOpa. In fact, the amount of carbon deposited followed the reverse order observed for the total amount of basic sites (Table 5).

This result suggested that the higher basicity of the support minimized carbon deposition.

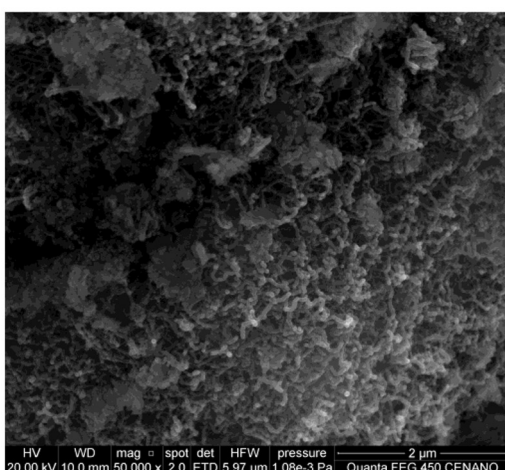
According to the mechanism proposed, ethanol adsorbs dissociatively as ethoxy species on a Lewis acid sites-strong basic sites pairs. Then, ethoxy species is dehydrogenated, producing acetaldehyde that may be further oxidized to acetate species with either surface oxygen or hydroxyl group of the support [8]. These acetate species may be decomposed to CH_x and carbonate species and finally CO₂. The unbalance between the rate of the decomposition of acetate species to CO₂ and CH_x species and the rate of desorption of CH_x species as CH₄ leads to the accumulation of carbon deposits. This in turn obstructs the metal-support interface, which results in catalyst deactivation, because the acetate demethanation reaction is promoted by the metal. As it is proposed for the SR of methane, increasing the basicity of the support increases the rate of carbon gasification reaction, decreasing carbon accumulation [10].

Metal sintering is also another possible cause of catalyst deactivation. Then, the changes in the Ni⁰ crystallite size during reduction and SR of ethanol reaction were monitored by *in situ* XRD. Table 7 listed the average crystallite size of Ni⁰ after reduction at 1023 K and after SR of ethanol reaction at 773 K for Ni supported catalysts. After reduction, the average crystallite size of Ni⁰ was approximately the same for all catalysts (7.9–10.7 nm). The Ni⁰ crystallite size remained unchanged during the reaction for all catalysts, indicating that Ni sintering does not occur during SR of ethanol at 773 K.

(A)



(B)



(C)

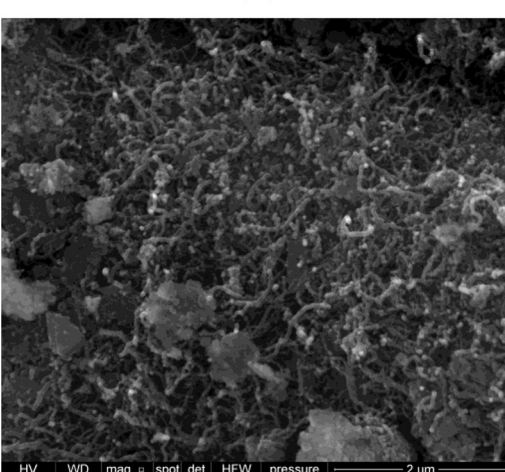


Fig. 10. SEM images of Ni/MgO samples after SR of ethanol at 773 K, using $\text{H}_2\text{O}/\text{ethanol}$ molar ratio of 3.0; (A) Ni/MgOpa; (B) Ni/MgOp; (C) Ni/MgOd.

Table 7

Average crystallite size of Ni^0 after reduction at 1023 K and after SR of ethanol reaction.

Sample	Condition	Crystallite size Ni^0 (nm)
Ni/MgOpa	Reduced to 750 °C	8.4
	Post SRE	8.9
Ni/MgOp	Reduced to 750 °C	10.7
	Post SRE	10.7
Ni/MgOd	Reduced to 750 °C	7.9
	Post SRE	7.3

Therefore, these results demonstrate that Ni/MgO catalysts deactivation is mainly due to carbon deposition.

Different strategies have been proposed to minimize or inhibit carbon formation such as the increase of water/ethanol ratio and the addition of oxygen to the feed [8]. Since Ni/MgOpa exhibited the lowest carbon formation for SR of ethanol with $\text{H}_2\text{O}/\text{ethanol} = 3.0$, this catalyst was tested on the SR of ethanol with a $\text{H}_2\text{O}/\text{ethanol}$ ratio of 10.0 and on the OSR of ethanol with an $\text{O}_2/\text{ethanol}$ ratio of 0.5. The results obtained were shown in Fig. 11.

Increasing the $\text{H}_2\text{O}/\text{ethanol}$ molar ratio increased the selectivity to H_2 and CO_2 and decreased the formation of CO and CH_4 . These results are likely due to the promotion of the water gas-shift and steam reforming of methane reactions in the presence of higher water content in the feed. In addition, it was also noticed that ethanol conversion only slightly decreased during reaction.

The addition of oxygen to the feed increased the ethanol conversion. Compared with SR, the selectivity to H_2 and CO decreased, whereas the formation of CO_2 increased during OSR. These results could be attributed to the combustion reaction. The simultaneous addition of O_2 and H_2O to the feed significantly improved catalyst stability.

TG analysis of the used catalysts after SR of ethanol with a $\text{H}_2\text{O}/\text{ethanol} = 10$ and OSR at 773 K was carried out and the amount of carbon formed is also listed in Table 6. Increasing the $\text{H}_2\text{O}/\text{ethanol}$ molar ratio significantly decreased the formation of carbon, whereas the addition of oxygen to the feed almost completely eliminated the deposition of carbon.

Increasing the $\text{H}_2\text{O}/\text{ethanol}$ molar ratio or the addition of oxygen to the feed promotes the gasification of carbon by water and the carbon oxidation, and this, in turn, decreases the catalyst deactivation rate through continuous carbon removal [8,16,44–47].

4. Conclusions

Ni supported on MgO catalysts were prepared by three different synthesis routes: precipitation followed by aging; precipitation and decomposition of the precursor salt. The preparation method of MgO significantly affected the total amount of basic sites and the reducibility of the sample. TPD of adsorbed CO_2 showed that the basicity followed the order: Ni/MgOpa > Ni/MgOp > Ni/MgOd. TPR profiles revealed the presence of NiO particles and a NiO–MgO solid solution, which was identified by XRD. The reducibility depended on the amount of NiO–MgO solid solution. TPR and XANES showed that the reducibility increased when the fraction of NiO particles increased. Ni/MgOpa exhibited the highest reduction degree.

Regardless the MgO preparation method, all Ni/MgO catalysts deactivated during SR of ethanol at 773 K. SEM and TG of post-reaction catalysts revealed that catalyst deactivation was mainly due to carbon deposition. However, the amount of carbon deposited varied significantly depending on the preparation method of MgO. Carbon amount formed during SR of ethanol decreased as the basic-

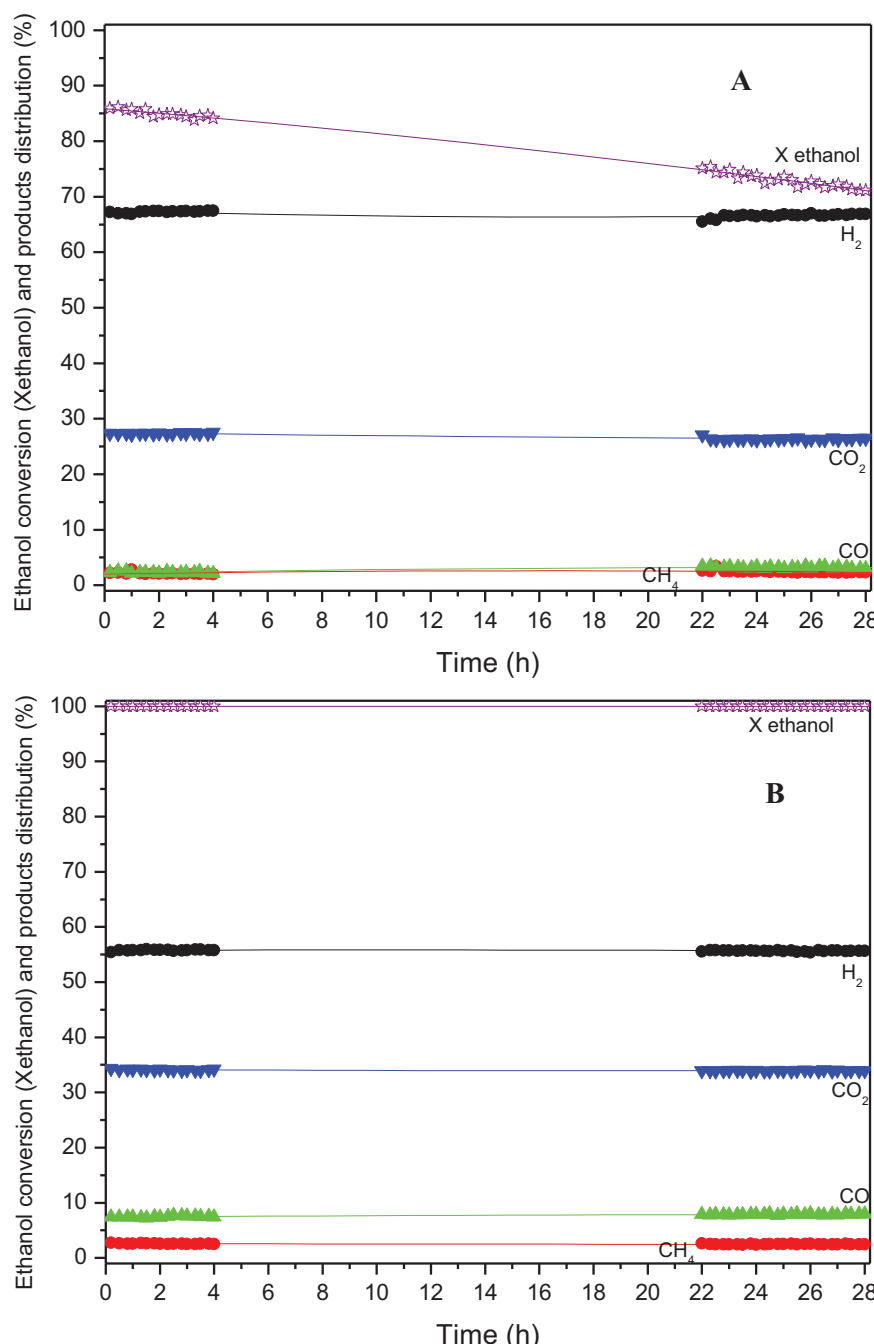


Fig. 11. Ethanol conversion and product distribution as a function of TOS over Ni/MgOpa catalyst for: (A) SR of ethanol at 773 K, using H₂O/ethanol molar ratio of 10.0; (B) OSR of ethanol at 773 K, using H₂O/ethanol/O₂ molar ratio = 3.0/1.0/0.5.

ity increased, which is likely due to the promotion of the rate of carbon gasification.

In order to minimize or inhibit carbon formation, the water/ethanol ratio of the feed was increased or oxygen was added to the feed. The increase of H₂O/ethanol molar ratio favored the water gas-shift and steam reforming of methane reactions. The addition of oxygen to the feed decreased the selectivity to H₂ due to the combustion reaction. Increasing the H₂O/ethanol molar ratio or the addition of oxygen to the feed promoted the gasification of carbon formed by water and the carbon oxidation, decreasing significantly carbon deposition and improving catalyst stability.

Acknowledgements

Gleiciele W. Tozzi and Raimundo C. Rabelo-Neto acknowledge the scholarships received from CAPES and FAPERJ. The group thanks LNLS for the assigned beamtime at XAFS-2 (proposal—16244) and XPD (proposal—17955) and for the valuable support to perform the XAFS studies.

References

- [1] R. Ramachandran, R.K. Menon, Int. J. Hydrg. Energy 23 (1998) 593–598.
- [2] J.H. Hirschenhofer, D.B. Stauffer, R.R. Engleman, M.G. Klett, Fuel Cell Handbook, 4th Ed., 1998.

- [3] A.V. Brigdwater, *Biomass Bioenergy* 38 (2012) 68–94.
- [4] M. Balakrishnana, E.R. Sacia, S. Sreekumara, G. Gunbas, A.A. Gokhale, C.D. Scown, F.D. Toste, A.T. Bell, *PNAS* (2015), <http://dx.doi.org/10.1073/pnas.1508274112>.
- [5] A. Haryanto, S. Fernando, N. Murali, S. Adhikari, *Energy Fuels* 19 (2005) 2098–2106.
- [6] P.D. Vaidya, A.E. Rodrigues, *Chem. Eng. J.* 117 (2006) 39–49.
- [7] M. Ni, Y.C. Leung, M.K.H. Leung, *Int. J. Hydrol. Energy* 32 (2007) 3238–3247.
- [8] L.V. Mattos, G. Jacobs, B.H. Davis, F.B. Noronha, *Chem. Rev.* 112 (2012) 4094–4123.
- [9] D.K. Liguras, D.I. Kondarides, X.E. Verykios, *Appl. Catal. B* 43 (2003) 345–354.
- [10] D.L. Trimm, *Catal. Today* 49 (1999) 3–10.
- [11] F. Frusteri, S. Freni, L. Spadaro, V. Chiodo, G. Bonura, S. Donato, S. Cavallaro, *Catal. Commun.* 5 (2004) 611–615.
- [12] F. Frusteri, S. Freni, V. Chiodo, S. Donato, G. Bonura, S. Cavallaro, *Int. J. Hydrol. Energy* 31 (2006) 2193–2199.
- [13] F. Frusteri, S. Freni, *J. Power Sources* 173 (2007) 200–209.
- [14] M.S. Batista, R.K.S.S. Santos, E.M. Assaf, E.A. Ticianelli, *J. Power Sources* 124 (2003) 99–103.
- [15] J. Llorca, N. Homs, J. Sales, P.R. Piscina, *J. Catal.* 209 (2002) 306–317.
- [16] A.N. Farsikostas, D.I. Kondarides, X.E. Verykios, *Catal. Today* 75 (2002) 145–155.
- [17] S. Cavallaro, N. Mondello, S. Freni, *J. Power Sources* 102 (2001) 198–204.
- [18] F. Frusteri, S. Freni, V. Chiodo, L. Spadaro, O. Di Blasi, G. Bonura, S. Cavallaro, *Appl. Catal. A* 270 (2004) 1–7.
- [19] N. Palmeri, S. Cavallaro, V. Chiodo, S. Freni, F. Frusteri, J.C.J. Bart, *Int. J. Hydrol. Energy* 32 (2007) 3335–3342.
- [20] Q. Shi, C. Liu, W. Chen, *J. Rare Earths* 27 (2009) 948–954.
- [21] A.O. Menezes, P.S. Silva, E.P. Hernández, L.E.P. Borges, M.A. Fraga, *Langmuir* 26 (2010) 3382–3387.
- [22] L. Vegard, *Z. Phys.* 5 (1921) 17–26.
- [23] M. Newville, *J. Synchrotron Radiat.* 8 (2001) 96–100.
- [24] E. Ruckenstein, Y.H. Hu, *Appl. Catal. A* 154 (1997) 185–205.
- [25] V.K. Díez, C.R. Apesteguía, J.I. Di Cosimo, *J. Catal.* 240 (2006) 235–244.
- [26] F. Arena, F. Frusteri, A. Parmaliana, L. Plyasova, A.N. Shmakov, *J. Chem. Soc. Faraday Trans.* 92 (1996) 469–471.
- [27] M. Nurunnabi, B. Li, K. Kunimori, K. Suzuki, K. Fujimoto, K. Tomishige, *Appl. Catal. A* 292 (2005) 272–280.
- [28] Y.G. Chen, K. Tomishige, K. Yokoyama, K. Fujimoto, *J. Catal.* 184 (1999) 479–490.
- [29] D. Li, L. Wang, M. Koike, Y. Nakagawa, K. Tomishige, *Appl. Catal. B* 102 (2011) 528–538.
- [30] O. Yamazaki, K. Tomishige, K. Fujimoto, *Appl. Catal. A* 136 (1996) 49–56.
- [31] J. Li, R. Li, C. Wang, C. Huang, W. Weng, H. Wan, *Chin. J. Catal.* 30 (2009) 714–716.
- [32] S.D. Robertson, B.D. McNicol, J.H. De Baas, S.C. Kloet, *J. Catal.* 37 (1975) 424–431.
- [33] B. Scheffer, P. Molhoek, J.A. Moulijn, *Appl. Catal.* 46 (1989) 11–30.
- [34] W.S. Dong, H.S. Roh, K.W. Jun, S.E. Park, Y.S. Oh, *Appl. Catal. A* 226 (2002) 63–72.
- [35] M. Ran, W. Chu, Y. Liu, D. Liu, C. Zhang, J. Zheng, *J. Energy Chem.* 23 (2014) 781–788.
- [36] B.L. Augusto, L.O.O. Costa, F.B. Noronha, R.C. Colman, L.V. Mattos, *Int. J. Hydrol. Energy* 37 (2012) 12258–12270.
- [37] F. Frusteri, S. Freni, V. Chiodo, S. Donato, G. Bonura, S. Cavallaro, *Int. J. Hydrol. Energy* 31 (2006) 2193–2199.
- [38] A. Parmaliana, F. Arena, F. Frusteri, N. Giordano, *J. Chem. Soc. Faraday Trans.* 86 (1990) 2663–2669.
- [39] J.L. Ewbank, L. Kovarik, F.Z. Diallo, C. Sievers, *Appl. Catal. A: Gen.* 494 (2015) 57–67.
- [40] T.S. Moraes, R.C.R. Neto, M.C. Ribeiro, L.V. Mattos, M.K.X. Verykios, F.B. Noronha, *Top. Catal.* 58 (2015) 281–294.
- [41] M. Bolognini, F. Cavanis, D. Scagliarini, C. Flego, C. Perego, M. Saba, *Catal. Today* 75 (2002) 103–111.
- [42] J.I. Cosimo, V.K. Díez, M. Xu, E. Iglesia, C.R. Apesteguía, *J. Catal.* 178 (1998) 499–510.
- [43] Z.Y. Ma, C. Yang, W. Wei, W.H. Li, Y.H. Sun, *J. Mol. Catal. A: Chem.* 227 (2005) 119–124.
- [44] V. Klouz, V. Pierro, P. Denton, H. Katz, J.P. Lisse, S. Bouvot-Mauduit, C. Mirodatos, *J. Power Sources* 105 (2002) 26–34.
- [45] S.M. Lima, A.M. Silva, L.O.O. Costa, J.M. Assaf, G. Jacobs, B.H. Davis, L.V. Mattos, F.B. Noronha, *Appl. Catal. A* 377 (2010) 181–190.
- [46] S.M. Lima, I.O. Cruz, G. Jacobs, B.H. Davis, L.V. Mattos, F.B. Noronha, *J. Catal.* 257 (2008) 356–368.
- [47] S.M. Lima, A.M. Silva, L.O.O. Costa, U.M. Graham, G. Jacobs, B.H. Davis, L.V. Mattos, F.B. Noronha, *J. Catal.* 268 (2009) 2.